



JGR Solid Earth

RESEARCH ARTICLE

10.1029/2020JB019525

Key Points:

- Receiver function harmonic conversions show pervasive dipping fault-parallel lithospheric fabric in Southern California
- Seismicity shows consistent northeast dips on profiles across major transform faults
- Non-Andersonian dipping fault geometry for strike-slip motion is likely due to tectonic inheritance

Supporting Information:

- Supporting Information S1

Correspondence to:

V. Schulte-Pelkum,
vera.schulte-pelkum@colorado.edu

Citation:

Schulte-Pelkum, V., Ross, Z. E., Mueller, K., & Ben-Zion, Y. (2020). Tectonic inheritance with dipping faults and deformation fabric in the brittle and ductile Southern California crust. *Journal of Geophysical Research: Solid Earth*, 125, e2020JB019525. <https://doi.org/10.1029/2020JB019525>

Received 5 FEB 2020

Accepted 22 JUN 2020

Accepted article online 25 JUN 2020

Tectonic Inheritance With Dipping Faults and Deformation Fabric in the Brittle and Ductile Southern California Crust

Vera Schulte-Pelkum^{1,2} , Zachary E. Ross³ , Karl Mueller², and Yehuda Ben-Zion⁴ 

¹Cooperative Institute for Research in Environmental Sciences (CIRES), University of Colorado Boulder, Boulder, CO, USA, ²Department of Geological Sciences, University of Colorado Boulder, Boulder, CO, USA, ³Seismological Laboratory, California Institute of Technology, Pasadena, CA, USA, ⁴Department of Earth Sciences and Southern California Earthquake Center, University of Southern California, Los Angeles, CA, USA

Abstract Plate motions in Southern California have undergone a transition from compressional and extensional regimes to a dominantly strike-slip regime in the Miocene. Strike-slip motion is most easily accommodated on vertical faults, and major transform fault strands in the region are typically mapped as near vertical on the surface. However, some previous work suggests that these faults have a dipping geometry at depth. We analyze receiver function arrivals that vary harmonically with back azimuth at all available broadband stations in the region. The results show a dominant signal from contrasts in dipping foliation as well as dipping isotropic velocity contrasts from all crustal depths, including from the ductile middle to lower crust. We interpret these receiver function observations as a dipping fault-parallel structural fabric that is pervasive throughout the region. The strike of these structures and fabrics is parallel to that of nearby fault surface traces. We also plot microseismicity on depth profiles perpendicular to major strike-slip faults and find consistently NE dipping features in seismicity changing from near vertical (80–85°) on the Elsinore Fault in the Peninsular Ranges to 60–65° slightly further inland on the San Jacinto Fault to 50–55° on the San Andreas Fault. Taken together, the dipping features in seismicity and in rock fabric suggest that preexisting fabrics and faults may have acted as strain guides in the modern slip regime, with reactivation and growth of strike-slip faults along northeast dipping fabrics both above and below the brittle-ductile transition.

Plain Language Summary In Southern California, blocks of the Earth's crust move horizontally past each other along the San Andreas Fault and other major faults. Simple mechanics concepts dictate that such fault zones should be oriented vertically with depth. By looking at the locations of small earthquakes along the fault zones and from imaging texture in the rock using seismograms, we instead find that the fault zones tend to dip away from the vertical in the subsurface. They also parallel features and rock fabric formed in previous geological events. We conclude that the geological history of a region can control its deformation behavior in the present.

1. Introduction

The San Andreas Fault (SAF) is the main strand of the California plate boundary between the Pacific and North American plates. In Central California, strike-slip motion is focused on the SAF, and observations of deep seismicity and tremor in the lower crust suggest a vertical fault structure cutting through the entire crust (Becken et al., 2011; Johnson et al., 2013; Nadeau & Dolenc, 2005; Ryberg et al., 2010; Shelly, 2017; Shelly & Hardebeck, 2010). The fault geometry in Southern California is considerably more complex, with a long restraining bend in the SAF south of which current strain is partitioned onto several major strike-slip faults along with compressive and extensional structures associated with fault jogs. The main additional active strike-slip faults south of the Big Bend in the SAF include the San Jacinto Fault (SJF) and Elsinore Fault (EF) lying between the SAF and the coast to the southwest. The subsurface geometry of strike-slip faults including the SAF is generally treated as vertical outside of fault bends (e.g., Langenheim et al., 2005; Plesch et al., 2007), but recent work proposed dipping geometry at depth along most of the SAF including straight sections in Southern California (Barak et al., 2015; Fuis et al., 2012, 2017;

Qiu et al., 2019; Share et al., 2019) and for parts of the SJF (Ross et al., 2017), with all dips to the northeast except for a SW dipping segment just south of the central SAF (Fuis et al., 2012).

Nonvertical geometries of strike-slip faults are of interest because ground shaking is increased on the hanging wall compared to a vertical geometry (Fuis et al., 2017; Oglesby et al., 2000). Such geometries may contain information on older fault networks that may influence present-day deformation behavior. They also affect the interpretation of geodetic data (e.g., Dair & Cooke, 2009; Fattaruso et al., 2014; Fialko, 2006; Lindsey & Fialko, 2013), and geodetic studies have inferred nonvertical fault geometry of the southern SAF with dip angles of 50° near the northern end of the Salton Sea, steepening somewhat to the south (Tymofyeyeva et al., 2019; Tymofyeyeva & Fialko, 2018). Development of a nonvertical strike-slip fault has previously been interpreted as recording the reactivation of a prior dipping thrust or normal fault (Avouac et al., 2014; Sato et al., 2015). Dipping geometries on the SJF and EF have also been suggested as a consequence of inheritance from the shallowly dipping Western Salton Detachment fault (Dorsey et al., 2012; Mason et al., 2017). Inheritance of preexisting faults from past deformation regimes can influence the evolution of faults that accommodate strain in response to a change in plate motion, here related to subduction of an oceanic spreading ridge followed by an inboard jump of the transform system (Atwater & Stock, 1998). Inheritance and reactivation can also be related to older rock fabrics or rheological boundaries such as the edges of batholiths. Dip on the SAF may be due to fault localization along the boundary of a previously underthrust mafic Pacific plate under the North American plate in the region of the San Gorgonio to Cajon Passes and southern SAF (Barak et al., 2015; Fuis et al., 2017). Wang et al. (2020) found strong midcrustal negative radial surface wave anisotropy south of the SAF in Southern California and attribute it to preexisting fabric with either steeply dipping schists or gently dipping plagioclase-rich foliation.

An additional open question is how faults root and are connected between the brittle crust and the ductile lower crust and lithospheric mantle. It is unknown whether major continental transform faults root into localized subvertical shear zones, coalesce into wider regional-scale shear zones, or root into metamorphic rock fabrics that accommodate a distribution of discretized shear zones (Bernard & Behr, 2017; Sibson, 1983; Titus et al., 2007) even though the latter is most likely an overly simplified end-member model. As in the brittle case, if earlier strain led to fabric development in the ductile lithosphere, such inherited ductile fabric may produce mechanical anisotropy and change the deformation response to applied stress. It is unknown how much strain is required to reset plastic lithospheric fabric under a new stress field (Vauchez et al., 2012). Ductile crustal and lithospheric fabric and shear zone geometry may in turn affect how faults are loaded at brittle depths (e.g., Bourne et al., 1998; Dolan et al., 2007; England & Jackson, 1989; Montési, 2004; Roy & Royden, 2000a, 2000b; Platt & Becker, 2010). Fault geometries near the brittle-ductile transition and deformation fabric at ductile depths are therefore of particular interest.

Our goal in this study is to investigate the geometry of faults and of shear zones and rock fabric below faults in Southern California using two types of data. The first data set consists of azimuthally varying arrivals in receiver functions that are generated from contrasts in dipping shear fabric or dipping isotropic interfaces (section 2). Previous anisotropic receiver function work focused on the lower crust (Porter et al., 2011) and on integrated shear fabric throughout the crust and uppermost mantle (Schulte-Pelkum & Mahan, 2014a) at a selected number of permanent stations. We present depth-dependent results throughout the lithosphere at all available permanent and temporary broadband stations. The second data set is the waveform-based, relocated Southern California catalog of earthquakes for 1981–2017 by Hauksson et al. (2012). We plot profiles showing the fine structure of seismicity across major fault strands and near the brittle-ductile transition in section 2. We synthesize the findings from seismicity and receiver function anisotropy in terms of tectonics, geodynamic memory, and the influence of geological history on present-day deformation via inheritance of faults and fabrics in section 4.

2. Receiver Function Arrivals From Anisotropic and Dipping Contrasts

Previous work using receiver functions in Southern California based on a sparser subset of stations suggested dipping foliation in the lower crust (Porter et al., 2011) and in the entire lithosphere (Schulte-Pelkum & Mahan, 2014a). If present-day strike-slip motion controls lithospheric fabric, one might expect vertical faults and vertical shear planes in this region rather than dipping ones. It is possible that thin

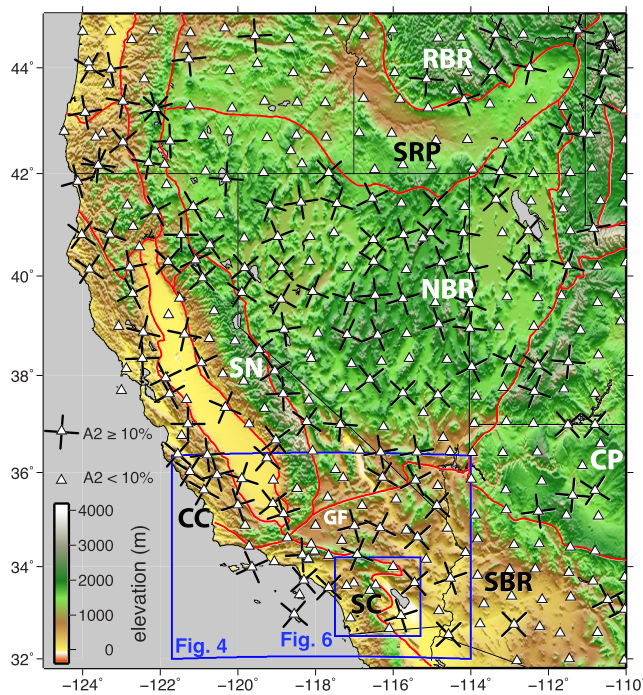


Figure 1. Map of stations in the EarthScope Transportable Array (white triangles) where the A_2 -periodic azimuthal signal from anisotropy exceeds (black bars) or does not exceed (triangle without bars) 10% of the receiver function amplitude. Black bars are fast and slow orientations averaged axially over the parts of the signal exceeding 10%. Red lines are physiographic province boundaries. Blue lines show extents of later figures. RBR: Rocky Mountain Basin and Range; SRP: Snake River Plain; NBR: Northern Basin and Range; SN: Sierra Nevada; CP: Colorado Plateau; CC: Central California; GF: Garlock Fault; SBR: Southern Basin and Range; SC: Southern California. Analysis details in Schulte-Pelkum and Mahan (2014a).

vertical shear zones below the resolution limit of receiver functions (i.e., $\ll 1$ km) cut through inherited fabric, but an explanation of why fault strikes are parallel to strikes of imaged dipping fabric is still necessary. Crustal layers with vertical foliation or horizontal lineation generate receiver function arrivals with π -periodic polarity (second azimuthal harmonic, A_2) changes in back azimuth (Brownlee et al., 2017; Levin & Park, 1998). In surface wave studies, such fabric is referred to as having azimuthal anisotropy (e.g. Lin, Ritzwoller, et al., 2011). Figure 1 displays which stations in the EarthScope Transportable Array show at least one A_2 -periodic arrival with an amplitude exceeding 10% horizontal to vertical amplitude ratio within the first 8 s (lithospheric depths), requiring a lithospheric layer with strong vertical foliation or horizontal lineation (Schulte-Pelkum & Mahan, 2014a). A strong A_2 signal is plotted as a station with a cross. The cross bars denote the fast and slow orientation of anisotropy averaged over depths exceeding 10% signal amplitude—fast versus slow orientations are degenerate in this analysis unless additional assumptions are made. The A_2 signal dominates in the Northern Basin and Range and the coastal ranges of Central California, while it is weak (stations without crosses) in the Snake River Plain, the Colorado Plateau, the Southern Basin and Range, and the Sierra Nevada (Figure 1). Since the transform plate boundary runs through Southern California into the Central California coastal ranges, it is surprising that Southern California shows a weaker azimuthal anisotropy signal than the latter region. Previous studies (Porter et al., 2011; Schulte-Pelkum & Mahan, 2014a) also suggest dominant dipping rather than vertical foliation in Southern California. In the present study, we analyze all available permanent and temporary stations from 2004–2017, forming a denser data set, for signatures of contrasts in dipping foliation and dipping isotropic contrasts in receiver functions.

2.1. Receiver Function Sensitivity to Anisotropic and Dipping Contrasts

Seismic anisotropy is expressed in receiver functions in two fundamentally different ways. One is the splitting of an S arrival after conversion from P ; the most commonly used is the P -to- S conversion from the Moho. We do not apply this method here, as it only provides an integrated measure of anisotropy over the travel path; it is therefore unlikely to accurately measure anisotropy from shear zones with limited thickness and may also not provide an accurate measure of bulk crustal anisotropy because of arrivals from thin anisotropic layers masquerading as bulk volume splitting (Liu & Park, 2017).

A more appropriate method in the presence of intracrustal anisotropic structure uses the azimuthally varying conversion from a contrast in anisotropy (Figure 2). A contrast in anisotropy of about 3% or a change in foliation orientation are sufficient to generate large-amplitude arrivals comparable to those from an average isotropic Moho contrast (Schulte-Pelkum & Mahan, 2014b). The conversions from such a contrast display characteristic polarity reversals with back azimuth on transverse as well as radial components (Jones & Phinney, 1998; Park & Levin, 2016; Savage, 1998; Schulte-Pelkum & Mahan, 2014b). The depth of such a contrast is given by the arrival time of the conversion in the receiver function (Figure 2), giving this method depth resolution, unlike splitting methods. Thin shear layers can also be resolved as long as conversions from the top and bottom of the layer are separated by close to a pulse width of the receiver function (usually 2–3 km thickness for receiver functions calculated at 1 Hz or higher). In many previous studies, arrivals are modeled directly to arrive at a usually nonunique model of anisotropy (Ozacar & Zandt, 2009; Porter et al., 2011; Vergne et al., 2003; Zandt et al., 2004). However, the harmonic behavior can be exploited directly (without forward modeling) to systematically separate signal from azimuthal anisotropy (horizontal symmetry axis) in the π -periodic amplitude component (A_2) and dipping foliation (plunging symmetry axis) in the

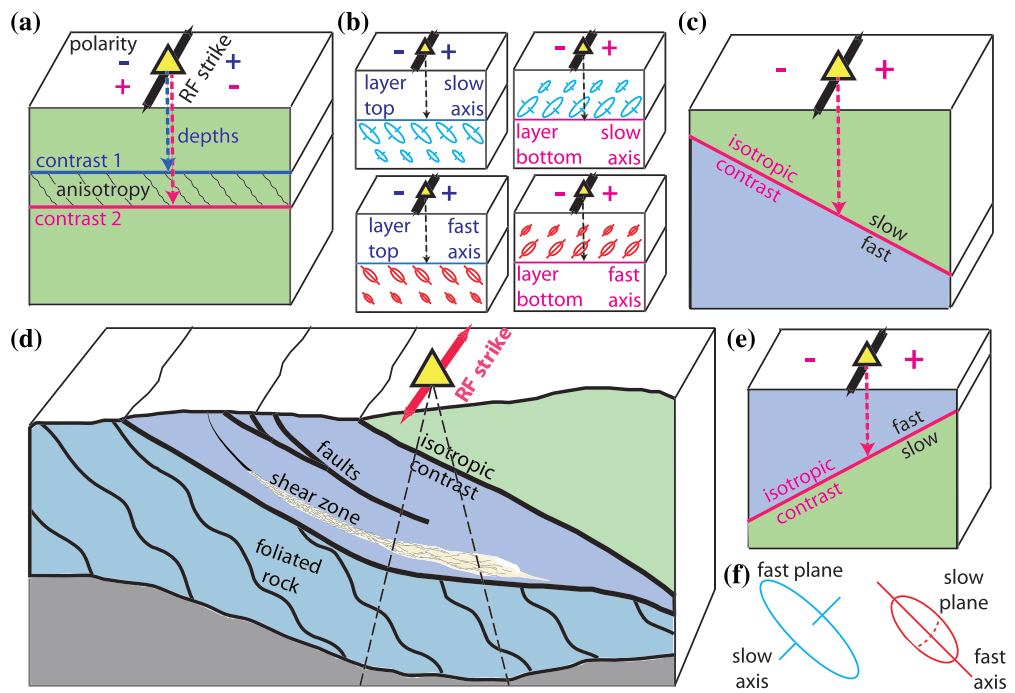


Figure 2. Illustration of sensitivity of receiver function to deformation-related structures in the lithosphere. (a) Horizontal layer with anisotropy (dipping foliation with fast V_p planes shown as wavy lines) embedded in isotropic layer with same average velocity (no isotropic velocity contrast). Receiver functions from different back azimuths at station (yellow triangle) show two arrivals with opposite polarity (+ and – signs) indicating foliation strike shown as black bar, one at a delay time corresponding to the depth of the blue contrast (blue dashed arrow), another from depth of the red contrast (red dashed arrow). (b) Illustration of tradeoffs between sense of foliation dip, anisotropic symmetry (fast- or slow-axis symmetry approximation), and whether an arrival is generated at the top or bottom of a layer with stronger anisotropy, with pattern symbols explained in (f). All four cases generate the same polarity reversal pattern (+ positive, – negative conversion amplitude). (c) Dipping interface with contrast in isotropic V_s ; black bar is strike registered at station; depth of red interface below station is found via delay time as in the anisotropic case. (d) Conceptual tectonic sketch after Fossen and Cavalcante (2017) and Harms et al. (2004) showing a composite of cases (a) and (b) within a compressional setting: Isotropic contrasts across faults (black lines), localized shear zone (beige), and distributed shear fabric (purple), with strike of these features picked up by receiver functions at station (yellow) from several depths; dashed lines show receiver function sampling cone. (e) Illustration of tradeoff in dip sense in the isotropic contrast case; this case generates the same polarity pattern as Case (c). (f) Explanation of symbols used in (b).

2π -symmetric component (A_1 , Bianchi et al., 2008, 2010; Brownlee et al., 2017; Liu & Park, 2017; Long et al., 2017; Schulte-Pelkum & Mahan, 2014a). Some studies focus on azimuthal anisotropy using the A_2 component because of an argument that the A_1 component is also sensitive to dipping isotropic contrasts (Savage, 1998). However, the sensitivity to plunging axis anisotropy is much higher than for horizontal axis anisotropy (Park & Levin, 2016; Schulte-Pelkum & Mahan, 2014a). The method used here solves for strike of a dipping isotropic contrast or strike of the plane perpendicular to the symmetry axis of anisotropy, whether that is a slow or fast axis (Figure 2). This strike and the depth of the contrast in velocity or anisotropy are the most robust observables (Schulte-Pelkum & Mahan, 2014a, 2014b). The sense of dip trades off with whether the anisotropy is best approximated by a fast or slow symmetry axis, and if the stronger anisotropy is above or below the interface (Figure 2). The amplitude of the A_1 arrival depends on the strength of the anisotropic or isotropic contrast as well as on the plunge of the symmetry axis or the isotropic contrast dip, with intermediate foliation dips generating larger conversion amplitudes than subhorizontal or subvertical foliation in the anisotropic case (Brownlee et al., 2017).

Figure 2 illustrates how strikes of dipping contrasts separating isotropic layers and of shear fabric foliation resulting from geological deformation processes are similar in orientation, such that the distinction between the two cases is secondary and is not made in this study.

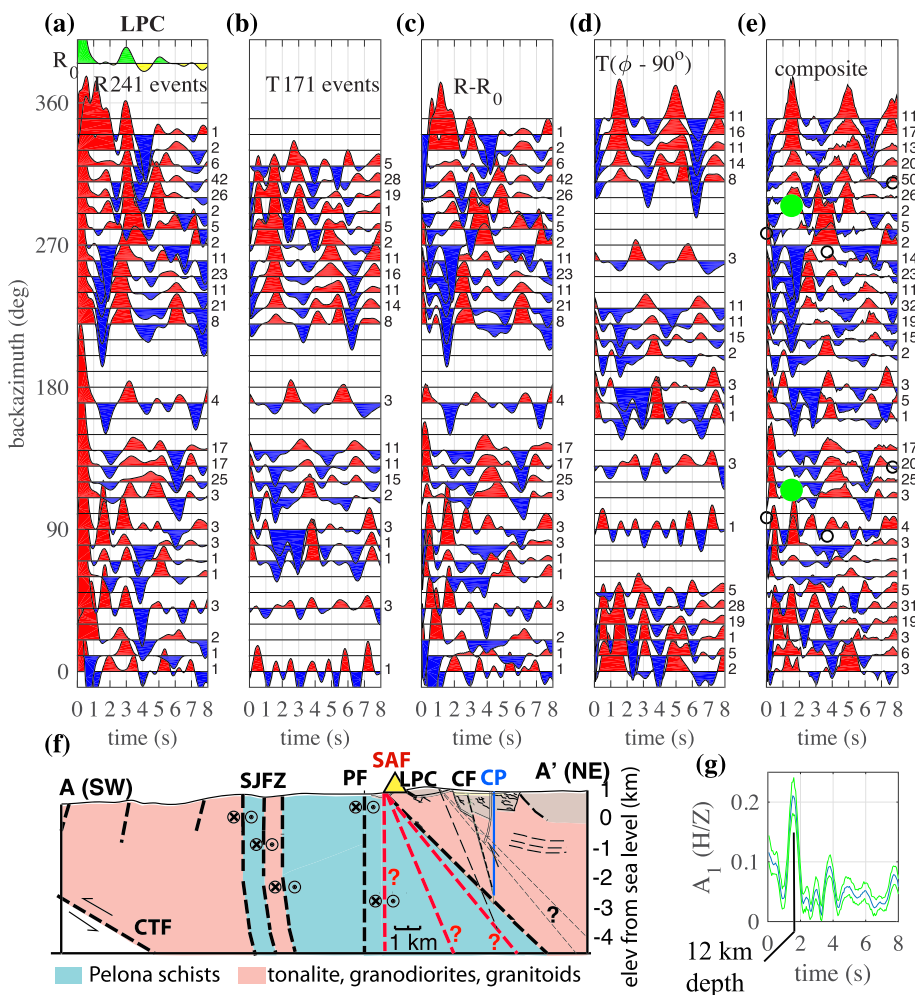


Figure 3. Receiver function analysis for example station LPC near Cajon Pass (Figure 4, bottom right). (a) Radial receiver functions binned by back azimuth after slowness correction; number of events per bin on the right of each trace. Amplitudes are non-normalized, same scale for all subplots. No azimuthal smoothing is applied. Trace on top is average over all azimuthal bins, R_0 . (b) Same as (a), but transverse component. (c) Radial component after R_0 was subtracted from each bin trace. (d) Transverse component after shifting traces by 90° in back azimuth. (e) Traces from c and d stacked together. Moving window harmonic analysis to determine amplitude and phase of first azimuthal harmonic A_1 is applied to this set (A_1 amplitude shown below in g). Green dots show strike of foliation inferred from maximum arrival, which parallels the SAF trace near the station (Figure 4). Black circles mark strikes of other maxima. (f) Geological cross section simplified from Forand et al. (2018) (profile location in Figure 4), based on Cajon Pass borehole (CP) samples, surface geology, and shallow reflection work. Blue line is borehole, dashed lines are inferred faults, and thin dashed lines metamorphic fabric; three alternative proposed dips were drawn by Forand et al. (2018) for SAF. CTF: Cucamonga Thrust Fault; PF: Punchbowl Fault; CF: Cleghorn Fault. (g) A_1 amplitude and 95% confidence interval on same time scale as (e).

2.2. Data and Analysis

We analyze broadband data from stations of the USArray, Southern California Seismic Network (SCSN), and Anza (Vernon, 1982) networks for the years 2004–2017, as well as from the 1997–1998 LARSE II experiment (Davis, 1998; Murphy et al., 2010; Zhu, 2002) and 2011 Salton Seismic Imaging Project (Barak et al., 2015; Klemperer, 2011). In order to maximize azimuthal coverage, we calculate receiver functions for P and P_{diff} arrivals from $30\text{--}150^\circ$ epicentral distance for all events with magnitude 5.0 and larger and apply an automated selection and quality control process (Schulte-Pelkum & Mahan, 2014a). From all events, we retain a mean of 6% of radial and 3% of the transverse component receiver functions with high signal-to-noise ratios and stable deconvolutions. We use the time domain algorithm by Ligorria and Ammon (1999) and a

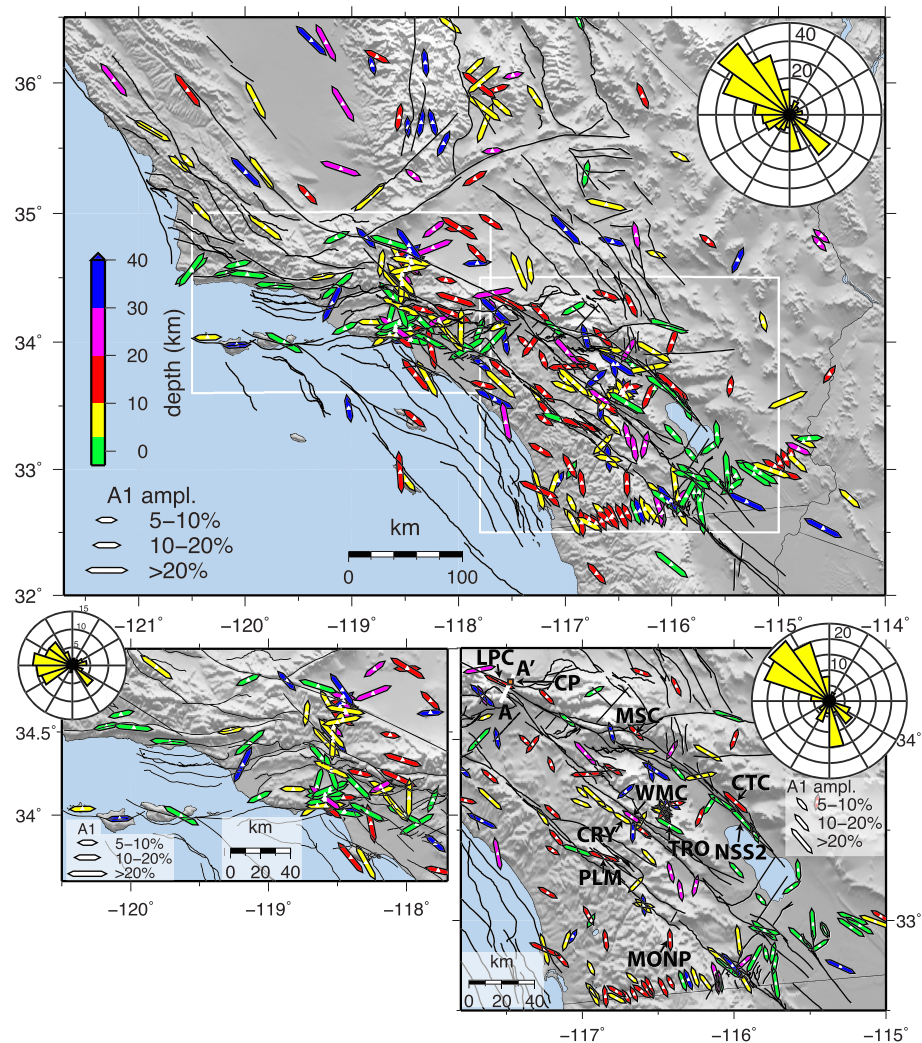


Figure 4. Map showing results for largest A_1 arrival at each station (white dot). See Figure 1 for location. Bar orientation shows the strike of dipping foliation or dipping isotropic interface, length varies with amplitude of the arrival, and color indicates depth of the converting contrast. Shading is relief, faults from SCEC CFM-5.2 (Plesch et al., 2007) in black. White outlines are magnified in lower maps. Circular insets are azimuthal histograms of strikes of the bars displayed in each corresponding map (bars on map are shown as axial orientations, while histograms show sense of strike using the right hand rule, e.g., NW strike implies dip to NE). Numbers in histograms show number of stations in each azimuthal bin. Note the predominance of NW strikes in overall area and in southern SAF-SJFZ-Elsinore Fault area (bottom right) and west strikes in the Transverse Ranges (bottom left). Strikes derived from our analysis are generally parallel those of nearby surface faults (histograms). Lower right map shows location of profile, borehole, and station in Figure 3, as well as station names for stations shown in Figures 6 and 7.

Gaussian filter factor of 3. Details of the processing and quality control methods are as in Schulte-Pelkum and Mahan (2014a).

The harmonic behavior is described in Schulte-Pelkum and Mahan (2014b) and the analysis method in Schulte-Pelkum and Mahan (2014a); we summarize it briefly here using station LPC near Cajon Pass as an example (Figure 3). After calculating radial and transverse component receiver functions, we apply slowness corrections so that the arrival times correspond to vertical incidence and amplitudes to a common incidence angle (Jones & Phinney, 1998). We then stack radial and transverse components separately in azimuthal 10° bins (Figures 3a and 3b). The radial component is a superposition of the isotropic flat-layered signal (termed R_0) that has no variation with back azimuth plus an azimuthally varying portion. We calculate the average radial receiver function over all bins as a proxy for R_0 and subtract it from each bin, so that the

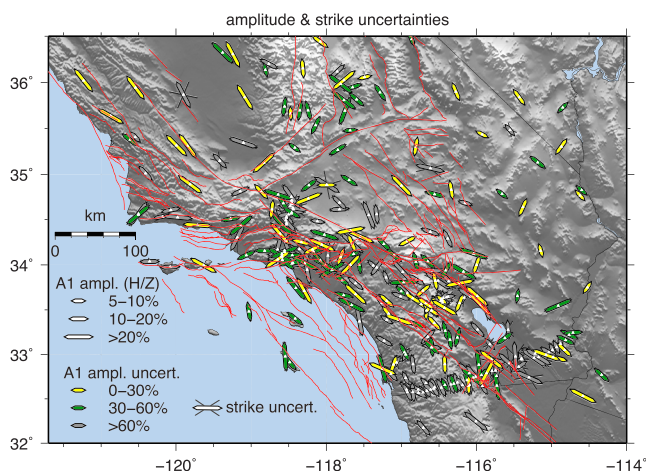


Figure 5. Same as Figure 4, except here color shows amplitude uncertainty based on bootstrap estimation, expressed as percent of the amplitude at each station. Strike uncertainty from bootstrapping is shown as thin gray lines (smaller than width of arrows for most stations).

0.2. Amplitudes in time domain receiver functions are absolute ratios of horizontal to vertical component amplitude, and 0.2–0.3 is the range of a strong Moho arrival amplitude. The strike of this arrival is 114° (green dots in Figure 3e), parallel to the strike of the SAF beneath the station (Figure 4c). The delay time of 1.6 s results in a depth of the contrast of 12.1 km when migrated with the 3-D velocity model profile at the station location. Figure 3f shows a simplified geological cross section (Forand et al., 2018) based on samples from the nearby Cajon Pass borehole (Figure 4c), surface geology, and shallow active source reflection results. The profile shows pervasive NE dipping structures. A contrast at 12 km beneath the station may be the downdip extension of the SJF Zone (SJFZ) if the latter has a listric geometry, or possibly connect to a range-bounding thrust fault further southwest (Figure 3f). Other arrivals are less prominent in amplitude (Figure 3g; delay time and strike marked as black circles in Figure 3e) and correspond to depths of 0.5, 30.5, and 70 km, with similar strikes. We focus on the largest arrival at each station as the best determined signal for the remainder of this paper.

2.3. Receiver Function Results

The amplitude, depth, and strike orientation of inferred foliation or dip from the largest arrival at each station are shown in Figure 4 on a map of the entire study area and two magnified subregions, along with azimuthal histograms of the strikes in each map region. NW strikes dominate the set from the entire area. Given the tradeoffs illustrated in Figure 2, additional assumptions are needed to infer the dominant dip sense. If we assume the signal is from either the top of a layer with dipping foliation with slow symmetry axis (Figure 2a), for instance, a schist or gneiss layer (Brownlee et al., 2017), or a dipping slow-over-fast isotropic interface (Figure 2c), then a NW strike would imply a foliation or isotropic contrast dip down to the NE. Larger amplitudes imply a stronger foliation or isotropic velocity contrast but can also be due to intermediate foliation dip angles, which generate conversions with larger amplitudes than those from contrast with subhorizontal or near-vertical foliation (Brownlee et al., 2017). The dominant NW-SE strike mirrors that of the dominant fault orientation, in particular that of the major transform faults in the region. In the Transverse Ranges (Figure 4, bottom left), fault orientations and receiver functions strikes rotate to E-W. In this region, an assumption of arrivals from the top of a layer with dipping foliation or a slow-over-fast isotropic contrast implies dips to the north, consistent with the geometry of thrust faulting located in the area. In the entire study region, the depths of the contrasts resulting in the largest A_1 arrival at each station are distributed throughout the lithosphere. No systematic changes of strike with depth are apparent.

Figure 5 shows the uncertainty in A_1 amplitude and strike based on bootstrap estimates. Bootstrapping is performed by eliminating azimuthal bins in separate 100 random instances before fitting the A_1 harmonic in each moving window. Azimuthal bin averages rather than individual receiver functions are eliminated to avoid undue weighting of densely sampled back azimuths. The amplitude uncertainty is given as the

azimuthally varying signal remains ($R - R_0$; Figure 3c). Assuming hexagonal symmetry (usually valid for crustal materials; Brownlee et al., 2017), in the case of plunging axis anisotropy the $R - R_0$ component will be the same as the transverse component (T) shifted by 90° clockwise in back azimuth ($\phi - 90^\circ$) as shown in Figure 3d; in the horizontal symmetry axis case, the azimuthal shift is 45° (Levin & Park, 1998; Schulte-Pelkum & Mahan, 2014a). To find the plunging axis anisotropy and isotropic dip signal, we stack $R - R_0$ and $T(\phi - 90^\circ)$ together in back azimuthal bins (Figure 3e). For all stations with azimuthal gaps smaller than 90°, we apply a moving window of 0.25 s length and solve for the first azimuthal harmonic in amplitude for each time window to obtain an A_1 signal amplitude and phase (Figures 3e and 3g). The phase of an amplitude peak is perpendicular to the strike of the dipping foliation contrast or dipping isotropic interface (Schulte-Pelkum & Mahan, 2014b, 2014a). The depth of the contrast is obtained by scaling the arrival time in the receiver function to depth using a V_p and V_s model between the converter and station.

In this study, we use the 3-D Southern California Earthquake Center (SCEC) Community Velocity Model CFM-H (Shaw et al., 2015). The largest amplitude arrival at station LPC is at 1.6 s, with an amplitude of

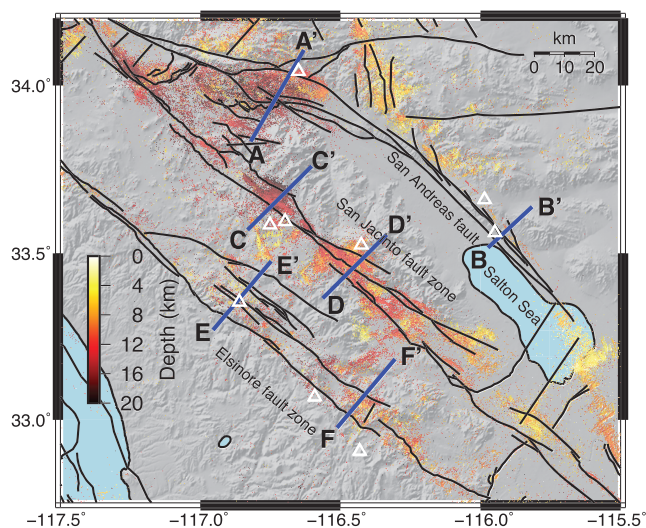


Figure 6. Map of epicenters and seismicity profile locations. Dots are epicenters in SCSN 1981–2017 catalog; color shows hypocenter depth. Relief in gray shade; black lines are fault surface traces from SCEC5 Community Fault Model (CFM; Plesch et al., 2007). Map area is marked in Figure 1 for wider regional context. Blue lines marked A–F are locations of cross-fault depth seismicity profiles in Figure 7. White open triangles are stations named in Figure 4 and shown in Figure 7.

the southern part of the study area that is dominated by strike-slip faulting, extending just into the Big Bend area to the north that includes thrust components Yang and Hauksson (2013) for the northernmost profile A–A'. Figure 6 displays prominent geographic trends in the depth of seismicity. The maximum earthquake depth gradually shallows from 20 km at the northwestern end near the San Jacinto mountains, to 10 km at the southeastern end south of the Salton Sea (supporting information Figure S1). This pattern defines the brittle-ductile transition, predominantly due to geothermal gradient changes along the profile (Doser & Kanamori, 1986), although other influences on rheology such as composition and fluid content are also likely (e.g., Burgmann & Dresen, 2008; Hauksson & Meier, 2019; Shinevar et al., 2018).

To better understand the geometry of seismicity across the primary fault zones within the Southern California plate boundary area, we examine a set of seismicity profiles roughly perpendicular to the SAF, SJF, and EF. Figure 7a shows a depth profile of seismicity along the southern SAF (SSAF) using the 1981–2017 SCSN catalog (top panel) and 2008–2017 QTM catalog (bottom panel). Relocations for the two catalogs were done independently using different methods and velocity models. The SCSN catalog (Hauksson et al., 2012) features a longer time span and captures some areas that were quiescent in 2008–2017, while the QTM catalog (Ross et al., 2019) covers a shorter time span but contains magnitudes down to much smaller values (nearly complete for events of magnitude above 0.3, compared to above 1.7 for the SCSN catalog). The vertical projections of the surface traces of the Banning and Mission Creek strands of the SSAF are denoted by the red dashed lines in Figure 7a. Green dashed lines show the average dip of the fault segments according to the SCEC CFM5.2 model. There is a clear northeast dipping structure to the seismicity, with dip values approximately 50–55° over the entire length of the profile. Fuis et al. (2017) argue based on this information and various other data sets and observations that the SSAF in this area as a whole dips 50–60° to the northeast. In addition to these observations, there is a broad area of microseismicity spanning about 15 km along the profile. A notable feature of this seismicity structure is that it is asymmetric across the fault. The QTM catalog shows more fine structure as expected from the lower magnitude threshold, while the SCSN catalog shows a planar dipping feature predating the QTM catalog in the northeastern portion of the profile. Station MSC is atop this feature and shows its largest A1 arrival from the bottom of the planar cluster, with a strike similar to that of the southern Banning strand (Figures 7 and 4).

Moving further to the southeast along the SSAF, Figure 7b shows a depth section which also exhibits a northeast dipping structure to the seismicity. Here, the seismicity is sparse but still exhibits a dip that projects

95% confidence interval, corresponding to two standard deviations if the distribution is normal. The strike uncertainty is given as the standard error of the strike in the bootstrapped distribution using circular statistics.

Strike uncertainties are small enough that they plot within the strike arrow for all but a few stations (Figure 5). Amplitude uncertainties vary widely and are higher for temporary stations with poorer azimuthal coverage. However, the similarity of inferred strikes between neighboring stations with smaller and larger nominal uncertainty, for instance, in the temporary more densely sampled linear experiments (e.g., the Salton Sea line in the southern part of the study area), suggests that the uncertainties calculated may be unduly pessimistic. We conclude that the receiver functions suggest dominant dipping fabric that is pervasive geographically and throughout the lithosphere in depth, with foliation or dip strikes largely parallel to currently active strike-slip and older inactive thrust or active faults.

3. Seismicity Profiles

We compare fault structures as illuminated by microseismicity to the dipping structural fabric imaged at depth using receiver functions by plotting hypocenters on depth profiles perpendicular to major transform faults. We use the entire relocated seismicity catalog of Hauksson et al. (2012), extended to the end of 2017. Figure 6 shows the geographic locations of the earthquakes and of seismicity depth profiles. This analysis covers

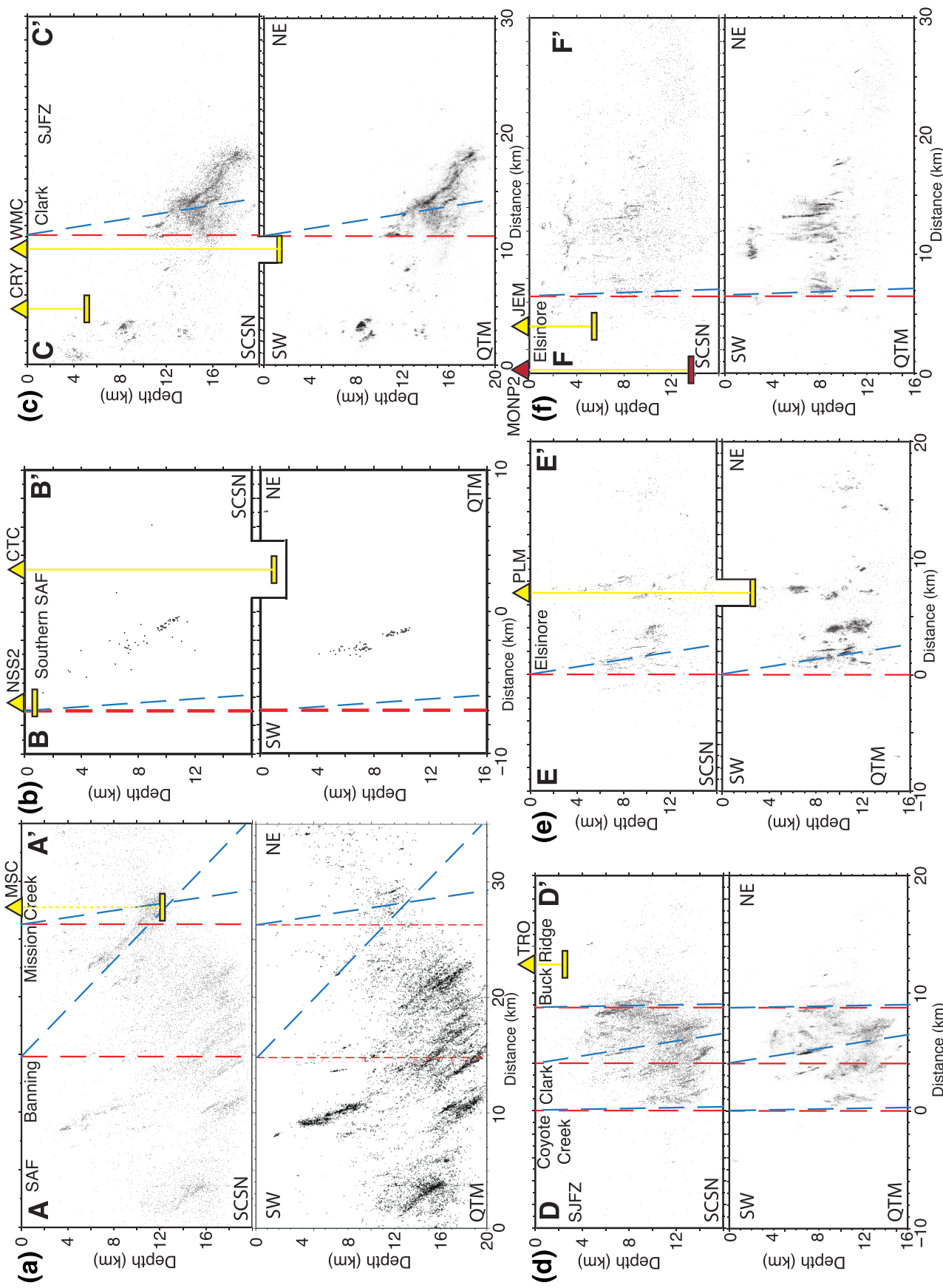


Figure 7. Seismicity profiles; profile locations marked in Figure 6. (a–f) Seismicity in each bottom panel from the 1981–2017 SCSN catalog; in each top panel from the 2008–2017 QTM catalog. Red dashed lines in profiles show vertical projection of fault surface traces; blue dashed lines show average dips of each fault segment; blue dashed lines show depths of maximum A1 arrival for the SCEC CFM-5 model. Triangles are locations of stations near profiles with low A1 uncertainty and arrivals near seismicogenic depths (station code given). Bars beneath stations show depths of maximum A1 arrival for the SCSN window. Yellow station and bar symbols are for arrivals with fault-parallel strike, orange for A1 arrival misoriented with surface faults. There is no vertical exaggeration in the profiles so that any dip angles are true dips. Seismicity shown is from within 5 km of each respective profile.

toward the surface trace of the fault. Figures S2 and S3 show additional densely spaced profiles that provides further evidence for this feature. Similar features were reported in Lin, Shearer, et al. (2007). Nearby stations show maximum A1 arrivals from depths and positions in line with the surface fault trace and the dip suggested by seismicity seen in the depth profile (Figure 7b), with strikes paralleling surface fault strike (Figures 4 and 6). A dip is also consistent with observations of head waves propagating along a dipping bimaterial fault in the region (Share & Ben-Zion, 2016). Here, the fault system has a slightly steeper dip than along profile A-A', and while the seismicity is shallower overall, the distributed seismicity here is fully on the northeast side of the SSAF. A NE dipping SAF was inferred at this location and south along the Salton Sea by Barak et al. (2015) using surface wave tomography.

Next, we move to the SJFZ, which is located to the southwest of the SSAF. Figure 7c contains a seismicity profile (3) across the Clark strand of the SJFZ through the Hot Springs segment. In this area, the event locations also define northeast dipping planes; however, they dip about 65–70°, compared with the dips of 50–60° observed for the seismicity on the SSAF. The band of seismicity flattens progressively from 12 to 17 km depth, to a greater extent than that in profile Figure 7a. Receiver function maximum arrivals from nearby stations bracket dipping seismicity features in depth Figure 7b, with strikes paralleling that of the fault trace.

The dipping pattern is also apparent in the complex trifurcation area of the SJFZ, which is located about 40 km to the southeast (Figure 7d). This area was studied in detail by Ross et al. (2017), who noted that in addition to the seismicity, the focal mechanisms at depth showed planes dipping about 70° to the northeast. They further suggested that the SJFZ transitions from dipping to near vertical above around 8 km depth based on the relative positions of the surface traces of the main faults and steeper focal mechanism and seismicity dips in the shallow structure. As with the SSAF, the bulk of the seismicity in these areas of the SJFZ is also predominantly located on the northeast side of the surface trace of the fault. The only nearby station shows a fault-parallel strike of its maximum A1 arrival with a depth shallower than the bulk of seismicity, to the northeast of the surface traces. Miocene age structures that are part of the Colorado River extensional corridor (Shirvell et al., 2009) formed low-angle, east rooting normal faults. One such fault is the Western Salton Detachment (Mason et al., 2017) that is offset by the SAF, SJFZ, and the EF from north to south (Dorsey et al., 2012). Mason et al. (2017) propose a transition from NE dipping shallow normal faulting to more steeply NE dipping strike-slip motion in the Pleistocene (8 Ma). Preexisting extensional structures may therefore act as strain guides during subsequent strike-slip faulting.

Finally, we examine two profiles across the EF zone (EFZ). While the EFZ has notably less seismicity than the other two faults, the same type of analysis is still possible. Figures 7e and 7f show seismicity profiles across the EFZ, which both indicate damage zones containing smaller cracks and faults northeast of the surface fault trace. Figure 7e shows features dipping about 80–85° to the northeast. A nearby station shows a maximum A1 arrival below seismogenic depths, with a strike parallel to that of the main fault trace to the southeast. Figure 7f shows features dipping from vertical to 85° in addition to a subhorizontal to shallowly NE dipping feature at 3–4 km depth. Nearby stations are to the southwest of the surface fault traces and show a shallow A1 maximum arrival with fault-aligned strike at one station, as well as a deep arrival with misaligned strike at another station, both away from the main clusters of seismicity. In both profiles, the damage zone and seismicity are asymmetric to the northeast of the surface trace of the fault. The shallowly dipping feature from 3–4 km depth in Profile F matches the position of the Western Salton Detachment fault shown by Dorsey et al. (2012). As in the case of the SJFZ, Dorsey et al. (2012) suggest a NE dip on the EFZ consistent with synthetic normal faults in the hanging wall of the top-to-the-east Western Salton Detachment system.

The dipping features are unlikely to be artifacts of the relocation procedure because the fabric of the seismicity exhibits these patterns over several different length scales and in both catalogs. These include narrow zones of activity that are relatively isolated, as well as more distributed damage zones that collectively define a persistent dipping pattern. While the relocation procedure performs a cluster analysis to identify which events to group together for relocation, there is no reason that the final locations should collapse to highly localized seismicity structures. Neither of the relocation methods impose planar features, which gives confidence to the results. The observations are furthermore generally consistent with regional focal mechanisms.

To summarize these results, all three of the major transform fault systems in Southern California exhibit narrow planar features of seismicity that dip to the northeast. The dip of each system progressively steepens

from about 50° in the northeast to about 80° in the southwest. This steepening may also occur toward the southeast, but the evidence for this is weaker from the seismicity. In addition, the damage zones that host these earthquakes are all strongly asymmetric across each fault system, with most of the earthquakes occurring on the northeast side. Together, these patterns consistently suggest that the observations are related to a regional pattern. Preexisting NE dipping extensional structures may have influenced the development of northeast dip on strike-slip faults (Dorsey et al., 2012; Mason et al., 2017; Shirvell et al., 2009).

4. Discussion: The Importance of Fault and Fabric Reactivation and Inheritance

The current tectonic regime in Southern California is one of transform motion on the plate boundary and regional N-S compressive stress (Heidbach et al., 2016; Kreemer et al., 2014; Yang & Hauksson, 2013). Thrust faulting in response to shortening across the Big Bend in the SAF occurs in the Western Transverse Ranges (Figure 4, bottom left) past the area of Profile A to Cajon Pass (Figure 6). In other areas, strike-slip faulting dominates (Yang & Hauksson, 2013). The maximum compressive stress in the crust is generally N-S with some regional variations and rotations with depth (Abolfathian et al., 2019, 2020). This suggests that microcracks in the brittle upper crust (above crack closure depths) would be expected to generally align N-S, parallel to the maximum compressive stress. Li and Peng (2017) analyzed shear wave splitting from local events within the seismogenic portion in the crust in Southern California. They found large deviations between the orientation of maximum compressive stress and the observed fast polarization orientation, with the latter rotating to fault-parallel along large parts of the SAF, regions between the SJFZ and EF, the Western Transverse Ranges, and other areas. Li and Peng (2017) concluded that the signal from present-day compression was affected by older structural features generating anisotropy.

Our results extend previous observations in two aspects. First, the fault-parallel anisotropy is not limited to the seismogenic crust but extends through all lithospheric depths (Figure 4). Similar to the systematic alignment parallel to faults seen in the shallow crust by Li and Peng (2017), fault-parallel foliation and contrasts are not limited to the vicinity of major faults but appear pervasive through the entire region. Second, rather than finding vertical foliation or horizontal lineation (i.e., an A_2 signal) and vertical fault traces and boundaries as one may expect with Andersonian mechanics under transform deformation, our results show dominant dipping fabric, material contrasts, and faults throughout the region. The strikes of the dominant fabric vary along with the fault strike in each subregion. Various subregions in Southern California have undergone rotation and translation and can be identified as blocks based on this kinematic history as in Porter et al. (2011). For instance, the rotated Western Transverse Ranges block (Figure 4, bottom left) shows E-W oriented faults and imaged strikes (Figure 4, bottom left strike histogram) compared to NW-SE strikes in the rest of the area. Additionally, we note that fault-parallel fabrics are present in blocks currently thought to be nondeforming based on geodesy (e.g., Kreemer et al., 2014), such as in the Peninsular Ranges near the international border with Baja California. We interpret these observations as indicating that Southern California contains a regional fabric. The regional fabric includes aligned shear zones and contrasts between isotropic bodies, that is, a regional-scale tectonic grain that is likely formed by older dipping fabrics related to earlier episodes of compressional or extensional tectonics as well as the present-day region-wide deformation regime.

Much like the small-scale examples of inherited fabric and reactivation discussed by Dorsey et al. (2012) and Mason et al. (2017) in the case of the EF and SJF influenced by the Western Salton Detachment Fault, pre-existing fabric, fault structures, and shear zones from previous compressional and extensional regimes likely affect the development and geometry of present-day transform faults across the region. Exhumed shear zones in the area show evidence for reactivation of Mesozoic thrusts in Cenozoic normal faulting in California and elsewhere (Goodwin & Wenk, 1995; Todd et al., 1988). Langenheim et al. (2004) propose that the geometry and path of the present-day SJF was dictated by a preexisting physical property contrast and that earthquakes on the fault continue to nucleate along this discontinuity. Detailed seismic imaging studies show that the main strike-slip faults in Southern California are associated with prominent lithology contrasts (e.g., Fang et al., 2016; Qiu et al., 2019; Share & Ben-Zion, 2016, 2018; Share et al., 2019). Here, we take this concept of inheritance further and propose that the Southern California region contains a pervasive rock fabric throughout the lithosphere. Present-day faults and deformation align along strikes dictated by this

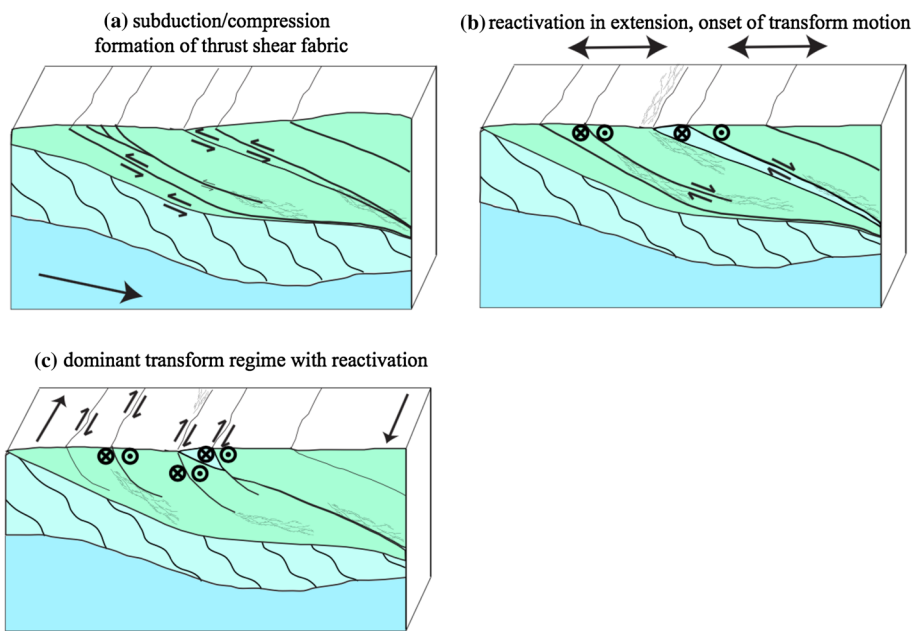


Figure 8. Conceptual illustration of the dominance of inherited structures and fabric on present-day tectonic fabric in Southern California. (a) Compressional regime during Farallon subduction (some reactivation of Mesozoic thrusts in extension). (b) Reactivation of compressional structures during extension; exhumation of some shear zones and deeper units; onset of transform deformation. (c) Dominant transform regime with dipping structures and fabric from the inherited compressional and extensional geometries. Location, strike, and dip of active structures in each regime are influenced by inherited prior structures and fabric.

inherited fabric, leading to geometries such as dipping strike-slip faults that would be energetically unfavorable in an isotropic homogeneous medium.

Figure 8 illustrates this concept with a loose tie to previous tectonic states and ages. A long history of shortening in the Mesozoic generated NE dipping thrust fabric and faults (Figure 8a). Thrusts were then overprinted and possibly reactivated during Miocene extension as normal faults (Goodwin & Wenk, 1995; Todd et al., 1988; Figure 8b). Late Miocene initiation of transform motion exploited the same NW-SW striking features and fabric, leading to dipping strike-slip fault structures parallel to the inherited fabric (Figure 8c). We propose that present-day faulting and deformation are thus affected by inherited structure. This observation has broad implications on the modeling and interpretation of present-day continental lithospheric deformation, faulting, and fault loading. To treat these processes accurately, it may be necessary to not only consider present-day stress but also take into account preexisting faults and rock fabric from past deformation. The pervasive nature of such fabric in Southern California implies that rather than considering individual shear zones, it may be sufficient to impose a preferential fabric (i.e., anisotropy of viscosity) when modeling deformation processes on a lithospheric scale. More sophisticated models should also explore the effect of major rheological boundaries associated with the Peninsular Ranges batholith and the Orocopia, Pelona, and Rand schists.

5. Conclusions

We analyzed receiver functions for conversions from contrasts in dipping foliation and from dipping isotropic interfaces and found such contrasts to be pervasive through lithospheric depths and laterally pervasive in Southern California. The strike of dipping fabric and contrasts tends to parallel that of surface faults. Seismicity profiles perpendicular to major transform faults show dipping features, with dips as well as damage zones preferentially to the northeast. The results are consistent with tomographic and fault zone head wave imaging studies.

If deformation in the lithosphere was controlled by present-day processes, and if inherited fabric was reset, one may expect vertical strike-slip faults and deformation fabric to be more developed in the immediate

vicinity of faults. We observe pervasive fabric that is not concentrated around faults and consistently dips to the northeast despite present-day dominant strike-slip deformation where shear would be assumed to be oriented along vertical planes were it not for older fabrics. Taken together with local geological reconstructions and other observations showing reactivation of inherited deformation features, we propose that present-day deformation in the brittle crust is partly controlled by older faults and inherited structures, and strain in the lower crust and uppermost mantle in modern transcurrent tectonics is also affected by regional lithospheric fabrics inherited from past deformation episodes.

Data Availability Statement

The facilities of the Southern California Earthquake Data Center (SCEDC) and of the IRIS Data Services (IRIS Data Management Center) were used for access to waveforms and related metadata used in this study (<https://doi.org/10.7914/SN/CI>, <https://doi.org/10.7914/SN/AZ>, and <https://doi.org/10.7914/SN/TA>). We used additional temporary network data from the LARSE (https://doi.org/10.7914/SN/XN_1998) and SSIP (https://doi.org/10.7914/SN/XD_2011) experiments. Data were retrieved via SOD (Owens et al., 2004). Seismicity catalogs are available at https://service.scedc.caltech.edu/eq-catalogs/date_mag_loc.php for the SCSN catalog and at <https://scedc.caltech.edu/research-tools/QTMCatalog.html> for the QTM catalog.

Acknowledgments

IRIS Data Services are funded through the Seismological Facilities for the Advancement of Geoscience and EarthScope (SAGE) Proposal of the National Science Foundation (NSF) under Cooperative Agreement EAR-1261681. The SCEDC and SCSN are funded through U.S. Geological Survey Grant G10 AP00091. This research was funded by NSF Grants EAR 1927246, 1735890, 1251193, and 1841315, and by Southern California Earthquake Center (SCEC) Grant 17097 (based on NSF Cooperative Agreement EAR-0529922 and USGS Cooperative Agreement 07HQAG0008). We thank P. Share for extracting 3-D velocity models, S. Marshall for providing fault summary data for the SCEC CFM-5.2 fault model, K. Mahan and M. Frothingham for discussions, and C. Condit for a basic sketch used in Figure 8. Comments by Editor I. Manighetti and two anonymous reviewers helped improve the paper significantly.

References

- Abolfathian, N., Martinez-Garzon, P., & Ben-Zion, Y. (2019). Spatiotemporal variations of stress and strain parameters in the San Jacinto Fault Zone. *Pure and Applied Geophysics*, 176(3), 1145–1168. <https://doi.org/10.1007/s00024-018-2055-y>
- Abolfathian, N., Martinez-Garzon, P., & Ben-Zion, Y. (2020). Variations of stress parameters in the Southern California plate boundary around the South Central Transverse Ranges. *Journal of Geophysical Research: Solid Earth*, 125, e2020JB019482. <https://doi.org/10.1029/2020JB019482>
- Atwater, T., & Stock, J. (1998). Pacific North America plate tectonics of the Neogene southwestern United States: An update. *International Geology Review*, 40(5), 375–402. <https://doi.org/10.1080/00206819809465216>
- Avouac, J.-P., Ayoub, F., Wei, S., Ampuero, J.-P., Meng, L., Leprince, S., et al. (2014). The 2013, Mw 7.7 Balochistan earthquake, energetic strike-slip reactivation of a thrust fault. *Earth and Planetary Science Letters*, 391, 128–134. <https://doi.org/10.1016/j.epsl.2014.01.036>
- Barak, S., Klemperer, S. L., & Lawrence, J. F. (2015). San Andreas Fault dip, Peninsular Ranges mafic lower crust and partial melt in the Salton Trough, Southern California, from ambient-noise tomography. *Geochemistry Geophysics Geosystems*, 16, 3946–3972. <https://doi.org/10.1002/2015GC005970>
- Becken, M., Ritter, O., Bedrosian, P. A., & Weckmann, U. (2011). Correlation between deep fluids, tremor and creep along the central San Andreas fault. *Nature*, 480(7375), 87. <https://doi.org/10.1038/Nature10609>
- Bernard, R. E., & Behr, W. M. (2017). Fabric heterogeneity in the Mojave lower crust and lithospheric mantle in Southern California. *Journal of Geophysical Research*, 122, 5000–5025. <https://doi.org/10.1002/2017JB014280>
- Bianchi, I., Park, J., Agostinetti, N. P., & Levin, V. (2010). Mapping seismic anisotropy using harmonic decomposition of receiver functions: An application to Northern Apennines, Italy. *Journal of Geophysical Research*, 115, B12317. <https://doi.org/10.1029/2009JB007061>
- Bianchi, I., Piana Agostinetti, N., De Gori, P., & Chiarabba, C. (2008). Deep structure of the Colli Albani volcanic district (central Italy) from receiver function analysis. *Journal of Geophysical Research*, 113, B09313. <https://doi.org/10.1029/2007JB005548>
- Bourne, S. J., England, P. C., & Parsons, B. (1998). The motion of crustal blocks driven by flow of the lower lithosphere and implications for slip rates of continental strike-slip faults. *Nature*, 391(6668), 655–659. <https://doi.org/10.1038/35556>
- Brownlee, S. J., Schulte-Pelkum, V., Raju, A., Mahan, K., Condit, C., & Orlandini, O. F. (2017). Characteristics of deep crustal seismic anisotropy from a compilation of rock elasticity tensors and their expression in receiver functions. *Tectonics*, 36(9), 1835–1857. <https://doi.org/10.1002/2017TC004625>
- Burgmann, R., & Dresen, G. (2008). Rheology of the lower crust and upper mantle: Evidence from rock mechanics, geodesy, and field observations. *Annual Review of Earth and Planetary Sciences*, 36, 531–567. <https://doi.org/10.1146/annurev.earth.36.031207.124326>
- Dair, L., & Cooke, M. L. (2009). San Andreas fault geometry through the San Gorgonio Pass, California. *Geology*, 37(2), 119–122. <https://doi.org/10.1130/G25101A.1>
- Davis, P. (1998). Los Angeles region seismic experiment—Passive phase. International Federation of Digital Seismograph Networks.
- Dolan, J. F., Bowman, D. D., & Sammis, C. G. (2007). Long-range and long-term fault interactions in Southern California. *Geology*, 35(9), 855–858. <https://doi.org/10.1130/G23789A.1>
- Dorsey, R. J., Axen, G. J., Peryam, T. C., & Kairouz, M. E. (2012). Initiation of the Southern Elsinore Fault at similar to 1.2 Ma: Evidence from the Fish Creek-Vallecito Basin, Southern California. *Tectonics*, 31, TC2006. <https://doi.org/10.1029/2011TC003009>
- Doser, D. I., & Kanamori, H. (1986). Depth of seismicity in the Imperial Valley region (1977–1983) and its relationship to heat flow, crustal structure and the October 15, 1979, earthquake. *Journal of Geophysical Research*, 91(B1), 675–688.
- England, P., & Jackson, J. (1989). Active deformation of the continents. *Annual Review of Earth and Planetary Sciences*, 17, 197–226. <https://doi.org/10.1146/annurev.earth.17.1.197>
- Fang, H., Zhang, H., Yao, H., Allam, A., Zigmone, D., Ben-Zion, Y., et al. (2016). A new algorithm for three-dimensional joint inversion of body wave and surface wave data and its application to the Southern California plate boundary region. *Journal of Geophysical Research: Solid Earth*, 121, 3557–3569. <https://doi.org/10.1002/2015JB012702>
- Fattaruso, L. A., Cooke, M. L., & Dorsey, R. J. (2014). Sensitivity of uplift patterns to dip of the San Andreas Fault in the Coachella Valley, California. *Geosphere*, 10(6), 1235–1246. <https://doi.org/10.1130/GES01050.1>
- Fialko, Y. (2006). Interseismic strain accumulation and the earthquake potential on the southern San Andreas fault system. *Nature*, 441(7096), 968–971. <https://doi.org/10.1038/nature04797>

- Forand, D., Evans, J. P., Janecke, S. U., & Jacobs, J. (2018). Insights into fault processes and the geometry of the San Andreas fault system: Analysis of core from the deep drill hole at Cajon Pass, California. *Geological Society of America Bulletin*, 130(1-2), 64–92. <https://doi.org/10.1130/B31681.1>
- Fossen, H., & Cavalcante, G. C. G. (2017). Shear zones—A review. *Earth-Science Reviews*, 171, 434–455. <https://doi.org/10.1016/j.earscirev.2017.05.002>
- Fuis, G. S., Bauer, K., Goldman, M. R., Ryberg, T., Langenheim, V. E., Scheirer, D. S., et al. (2017). Subsurface geometry of the San Andreas Fault in Southern California: Results from the Salton Seismic Imaging Project (SSIP) and strong ground motion expectations. *Bulletin of the Seismological Society of America*, 107(4), 1642–1662. <https://doi.org/10.1785/0120160309>
- Fuis, G. S., Scheirer, D. S., Langenheim, V. E., & Kohler, M. D. (2012). A new perspective on the geometry of the San Andreas Fault in Southern California and its relationship to lithospheric structure. *Bulletin of the Seismological Society of America*, 102(1), 236–251. <https://doi.org/10.1785/0120110041>
- Goodwin, L. B., & Wenk, H. R. (1995). Development of phyllonite from granodiorite—Mechanisms of grain-size reduction in the Santa-Rosa Mylonite Zone, California. *Journal of Structural Geology*, 17(5), 689–697. [https://doi.org/10.1016/0191-8141\(94\)00093-F](https://doi.org/10.1016/0191-8141(94)00093-F)
- Harms, T. A., Brady, J. B., Burger, H. R., & Cheney, J. T. (2004). Advances in the geology of the Tobacco Root Mountains, Montana, and their implications for the history of the northern Wyoming Province. *Special Paper - Geological Society of America*, 377, 227–243.
- Hauksson, E., & Meier, M. (2019). Applying depth distribution of seismicity to determine thermo-mechanical properties of the seismogenic crust in Southern California: Comparing lithotectonic blocks. *Pure and Applied Geophysics*, 176, 1061–1081. <https://doi.org/10.1007/s00224-018-1981-z>
- Hauksson, E., Yang, W., & Shearer, P. M. (2012). Waveform relocated earthquake catalog for Southern California (1981 to June 2011). *Bulletin of the Seismological Society of America*, 102(5), 2239–2244. <https://doi.org/10.1785/0120120010>
- Heidbach, O., Rajabi, M., Reiter, K., Ziegler, M., & WSM Team (2016). World stress map database release 2016. GFZ Data Services, 1061–1081, <https://doi.org/10.5880/WSM.2016.001>
- Johnson, K. M., Shelly, D. R., & Bradley, A. M. (2013). Simulations of tremor-related creep reveal a weak crustal root of the San Andreas Fault. *Geophysical Research Letters*, 40, 1300–1305. <https://doi.org/10.1002/grl.50216>
- Jones, C. J., & Phinney, R. A. (1998). Seismic structure of the lithosphere from teleseismic converted arrivals observed at small arrays in the southern Sierra Nevada and vicinity, California. *Journal of Geophysical Research*, 103, 10,065–10,090.
- Klemperer, S. (2011). Passive seismic study of a magma-dominated rift: The Salton Trough. International Federation of Digital Seismograph Networks.
- Kreemer, C., Blewitt, G., & Klein, E. C. (2014). A geodetic plate motion and Global Strain Rate Model. *Geochemistry Geophysics Geosystems*, 15, 3849–3889. <https://doi.org/10.1002/2014GC005407>
- Langenheim, V. E., Jachens, R. C., Matti, J. C., Hauksson, E., Morton, D. M., & Christensen, A. (2005). Geophysical evidence for wedging in the San Gorgonio Pass structural knot, southern San Andreas fault zone, Southern California. *Geological Society of America Bulletin*, 117(11-12), 1554–1572. <https://doi.org/10.1130/B25760.1>
- Langenheim, V. E., Jachens, R. C., Morton, D. M., Kistler, R. W., & Matti, J. C. (2004). Geophysical and isotopic mapping of preexisting crustal structures that influenced the location and development of the San Jacinto fault zone, Southern California. *Geological Society of America Bulletin*, 116(9-10), 1143–1157. <https://doi.org/10.1130/B25277.1>
- Levin, V., & Park, J. (1998). *P-SH* conversions in layered media with hexagonally symmetric anisotropy: A cookbook. *Pure and Applied Geophysics*, 151, 669–697.
- Li, Z., & Peng, Z. (2017). Stress- and structure-induced anisotropy in southern California from two decades of shear wave splitting measurements. *Geophysical Research Letters*, 44, 9607–9614. <https://doi.org/10.1002/2017GL075163>
- Ligorria, J. P., & Ammon, C. J. (1999). Iterative deconvolution and receiver-function estimation. *Bulletin of the Seismological Society of America*, 89(5), 1395–1400.
- Lin, F. C., Ritzwoller, M. H., Yang, Y., Moschetti, M. P., & Fouch, M. J. (2011). Complex and variable crustal and uppermost mantle seismic anisotropy in the western United States. *Nature Geoscience*, 4, 55–61. <https://doi.org/10.1038/NGEO1036>
- Lin, G., Shearer, P. M., & Hauksson, E. (2007). Applying a three-dimensional velocity model, waveform cross correlation, and cluster analysis to locate Southern California seismicity from 1981 to 2005. *Journal of Geophysical Research*, 112, B12309. <https://doi.org/10.1029/2007JB004986>
- Lindsey, E. O., & Fialko, Y. (2013). Geodetic slip rates in the southern San Andreas Fault system: Effects of elastic heterogeneity and fault geometry. *Journal of Geophysical Research: Solid Earth*, 118, 689–697. <https://doi.org/10.1029/2012JB009358>
- Liu, Z., & Park, J. (2017). Seismic receiver function interpretation: Ps splitting or anisotropic underplating? *Geophysical Journal International*, 208(3), 1332–1341. <https://doi.org/10.1093/gji/ggw455>
- Long, M. D., Ford, H. A., Abrahams, L., & Wirth, E. A. (2017). The seismic signature of lithospheric deformation beneath eastern North America due to Grenville and Appalachian orogenesis. *Lithosphere*, 9(6), 987–1001. <https://doi.org/10.1130/L660.1>
- Mason, C. C., Spotila, J. A., Axen, G., Dorsey, R. J., Luther, A., & Stockli, D. F. (2017). Two-Phase exhumation of the Santa Rosa Mountains: Low- and high-angle normal faulting during initiation and evolution of the southern San Andreas Fault system. *Tectonics*, 36, 2863–2881. <https://doi.org/10.1002/2017TC004498>
- Montésí, L. G. J. (2004). Controls of shear zone rheology and tectonic loading on postseismic creep. *Journal of Geophysical Research: Solid Earth*, 109, B10404. <https://doi.org/10.1029/2003JB002925>
- Murphy, J. M., Fuis, G. S., Ryberg, T., Lutter, W. J., Catchings, R. D., & Goldman, M. R. (2010). Detailed *P*- and *S*-wave velocity models along the LARSE II Transect, Southern California. *Bulletin of the Seismological Society of America*, 100(6), 3194–3212. <https://doi.org/10.1785/0120090004>
- Nadeau, R. M., & Dolenc, D. (2005). Nonvolcanic tremors deep beneath the San Andreas Fault. *Science*, 307(5708), 389. <https://doi.org/10.1126/science.1107142>
- Oglesby, D. D., Archuleta, R. J., & Nielsen, S. B. (2000). The three-dimensional dynamics of dipping faults. *Bulletin of the Seismological Society of America*, 90(3), 616–628. <https://doi.org/10.1785/0119990113>
- Owens, T. J., Crotwell, H. P., Groves, C., & Oliver-Paul, P. (2004). SOD: Standing order for data. *Seismological Research Letters*, 75(4), 515–520.
- Ozacar, A. A., & Zandt, G. (2009). Crustal structure and seismic anisotropy near the San Andreas Fault at Parkfield, California. *Geophysical Journal International*, 178(2), 1098–1104. <https://doi.org/10.1111/j.1365-246X.2009.04198.x>
- Park, J., & Levin, V. (2016). Anisotropic shear zones revealed by backazimuthal harmonics of teleseismic receiver functions. *Geophysical Journal International*, 207(2), 1216–1243. <https://doi.org/10.1093/gji/ggw323>

- Platt, J. P., & Becker, T. W. (2010). Where is the real transform boundary in California? *Geochemistry Geophysics Geosystems*, 11, Q06013. <https://doi.org/10.1029/2010GC003060>
- Plesch, A., Shaw, J. H., Benson, C., Bryant, W. A., Carena, S., Cooke, M., et al. (2007). Community fault model (CFM) for Southern California. *Bulletin of the Seismological Society of America*, 97(6), 1793–1802. <https://doi.org/10.1785/0120050211>
- Porter, R., Zandt, G., & McQuarrie, N. (2011). Pervasive lower-crustal seismic anisotropy in Southern California: Evidence for underplated schists and active Tectonics. *Lithosphere*, 3(3), 201–220. <https://doi.org/10.1130/L126.1>
- Qiu, H., Lin, F.-C., & Ben-Zion, Y. (2019). Eikonal tomography of the Southern California plate boundary region. *Journal of Geophysical Research: Solid Earth*, 124, 9755–9779. <https://doi.org/10.1029/2019JB017806>
- Ross, Z. E., Hauksson, E., & Ben-Zion, Y. (2017). Abundant off-fault seismicity and orthogonal structures in the San Jacinto fault zone. *Science Advances*, 3(3), e1601946.
- Ross, Z. E., Trugman, D. T., Hauksson, E., & Shearer, P. M. (2019). Searching for hidden earthquakes in Southern California. *Science*, 364(6442), 767–771.
- Roy, M., & Royden, L. H. (2000a). Crustal rheology and faulting at strike-slip plate boundaries 1. An analytic model. *Journal of Geophysical Research*, 105(B3), 5583–5597.
- Roy, M., & Royden, L. H. (2000b). Crustal rheology and faulting at strike-slip plate boundaries 2. Effects of lower crustal flow. *Journal of Geophysical Research*, 105(B3), 5599–5613. <https://doi.org/10.1029/1999JB900340>
- Ryberg, T., Haberland, C., Fuis, G. S., Ellsworth, W. L., & Shelly, D. R. (2010). Locating non-volcanic tremor along the San Andreas Fault using a multiple array source imaging technique. *Geophysical Journal International*, 183(3), 1485–1500. <https://doi.org/10.1111/j.1365-246X.2010.04805.x>
- Sato, H., Kato, N., Abe, S., Van Horne, A., & Takeda, T. (2015). Reactivation of an old plate interface as a strike-slip fault in a slip-partitioned system: Median Tectonic Line, SW Japan. *Tectonophysics*, 644, 58–67. <https://doi.org/10.1016/j.tecto.2014.12.020>
- Savage, M. K. (1998). Lower crustal anisotropy or dipping boundaries: Effects on receiver functions and a case study in New Zealand. *Journal of Geophysical Research*, 103, 15,069–15,087.
- Schulte-Pelkum, V., & Mahan, K. H. (2014a). A method for mapping crustal deformation and anisotropy with receiver functions and first results from USArray. *Earth and Planetary Science Letters*, 402, 221–233. <https://doi.org/10.1016/j.epsl.2014.01.050>
- Schulte-Pelkum, V., & Mahan, K. H. (2014b). Imaging faults and shear zones using receiver functions. *Pure and Applied Geophysics*, 171(11), 2967–2991. <https://doi.org/10.1007/s00024-014-0853-4>
- Share, P.-E., & Ben-Zion, Y. (2016). Bimaterial interfaces in the south San Andreas Fault with opposite velocity contrasts NW and SE from San Gorgonio Pass. *Geophysical Research Letters*, 43, 10,680–10,687. <https://doi.org/10.1002/2016GL070774>
- Share, P.-E., & Ben-Zion, Y. (2018). A bimaterial interface along the northern San Jacinto Fault through Cajon Pass. *Geophysical Research Letters*, 45, 11,622–11,631. <https://doi.org/10.1029/2018GL079834>
- Share, P.-E., Guo, H., Thurber, C. H., Zhang, H., & Ben-Zion, Y. (2019). Seismic imaging of the southern California plate boundary around the south-central transverse ranges using double-difference tomography. *Pure and Applied Geophysics*, 176(3), 1117–1143. <https://doi.org/10.1007/s00024-018-2042-3>
- Shaw, J. H., Plesch, A., Tape, C., Suess, M. P., Jordan, T. H., Ely, G., et al. (2015). Unified structural representation of the Southern California crust and upper mantle. *Earth and Planetary Science Letters*, 415, 1–15. <https://doi.org/10.1016/j.epsl.2015.01.016>
- Shelly, D. R. (2017). A 15-year catalog of more than 1 million low-frequency earthquakes: Tracking tremor and slip along the deep San Andreas Fault. *Journal of Geophysical Research*, 122, 3739–3753. <https://doi.org/10.1002/2017JB014047>
- Shelly, D. R., & Hardebeck, J. L. (2010). Precise tremor source locations and amplitude variations along the lower-crustal central San Andreas Fault. *Geophysical Research Letters*, 37, L14301. <https://doi.org/10.1029/2010GL043672>
- Shinevar, W. J., Behn, M. D., Hirth, G., & Jagoutz, O. (2018). Inferring crustal viscosity from seismic velocity: Application to the lower crust of Southern California. *Earth and Planetary Science Letters*, 494, 83–91. <https://doi.org/10.1016/j.epsl.2018.04.055>
- Shirvell, C. R., Stockli, D. F., Axen, G. J., & Grove, M. (2009). Miocene-Pliocene exhumation along the west Salton detachment fault, Southern California, from (U-Th)/He thermochronometry of apatite and zircon. *Tectonics*, 28, TC2006. <https://doi.org/10.1029/2007TC002172>
- Sibson, R. H. (1983). Continental fault structure and the shallow earthquake source. *Journal of the Geological Society*, 140, 741–767. <https://doi.org/10.1144/gsjgs.140.5.0741>
- Titus, S. J., Medaris, L. G., Wang, H. F., & Tikoff, B. (2007). Continuation of the San Andreas fault system into the upper mantle: Evidence from spinel peridotite xenoliths in the Coyote Lake basalt, central California. *Tectonophysics*, 429(1-2), 1–20. <https://doi.org/10.1016/j.tecto.2006.07.004>
- Todd, V. R., Erskine, B. G., & Morton, D. M. (1988). Metamorphic and tectonic evolution of the northern Peninsular Ranges batholith, Southern California. In Ernst, W. G. (Ed.), *Metamorphic and crustal evolution of the Northern Peninsular Ranges Batholith, Southern California, Rubey Volume no. VIII*. Englewood Cliffs, New Jersey: Prentice-Hall.
- Tymofeyeva, E., & Fialko, Y. (2018). Geodetic evidence for a blind fault segment at the southern end of the San Jacinto fault zone. *Journal of Geophysical Research: Solid Earth*, 123, 878–891. <https://doi.org/10.1002/2017JB014477>
- Tymofeyeva, E., Fialko, Y., Jiang, J., Xu, X., Sandwell, D., Bilham, R., et al. (2019). Slow slip event on the southern San Andreas Fault triggered by the 2017 Mw 8.2 Chiapas (Mexico) earthquake. *Journal of Geophysical Research: Solid Earth*, 124, 9956–9975. <https://doi.org/10.1029/2018JB016765>
- Vauchez, A., Tommasi, A., & Mainprice, D. (2012). Faults (shear zones) in the Earth's mantle. *Tectonophysics*, 558, 1–27.
- Vergne, J., Wittlinger, G., Farra, V., & Su, H. (2003). Evidence for upper crustal anisotropy in the Songpan-Ganze (northeastern Tibet) terrane. *Geophysical Research Letters*, 30(11), 1552. <https://doi.org/10.1029/2002GL016847>
- Vernon, F. (1982). ANZA regional network. International Federation of Digital Seismograph Networks.
- Wang, K., Jiang, C., Yang, Y., Schulte-Pelkum, V., & Liu, Q. (2020). Crustal deformation in Southern California constrained by radial anisotropy from ambient noise adjoint tomography. *Geophysical Research Letters*, 47, e2020GL088580. <https://doi.org/10.1029/2020GL088580>
- Yang, W., & Hauksson, E. (2013). The tectonic crustal stress field and style of faulting along the Pacific North America Plate boundary in Southern California. *Geophysical Journal International*, 194(1), 100–117. <https://doi.org/10.1093/gji/ggt113>
- Zandt, G., Gilbert, H., Owens, T. J., Ducea, M., Saleaby, J., & Jones, C. H. (2004). Active foundering of a continental arc root beneath the southern Sierra Nevada in California. *Nature*, 431(7004), 41–46. <https://doi.org/10.1038/nature02847>
- Zhu, L. P. (2002). Deformation in the lower crust and downward extent of the San Andreas Fault as revealed by teleseismic waveforms. *Earth Planets and Space*, 54(11), 1005–1010. International Symposium on Slip and Flow Processes in and Below the Seismogenic Region, Sendai, Japan, Nov 05–08, 2001, <https://doi.org/10.1186/BF03353293>